

Dual Measurements of Temporal and Spatial Coherence of Light in a Single Experimental Setup using a Modified Michelson Interferometer

Mohit Kumar Singh^{1,a)} and Shouvik Datta^{1,b)}

¹Department of Physics & Centre for Energy Science, Indian Institute of Science Education and Research, Pune 411008, Maharashtra, India

Author(s) to whom correspondence should be addressed:

a) mohitkumar.singh@students.iiserpune.ac.in

b) shouvik@iiserpune.ac.in

Abstract

An experimental technique is developed to simultaneously measure both temporal and spatial coherences of a light source by altering a standard Michelson interferometer, which has been primarily used for measuring temporal coherence only. Instead of using simple plane mirrors, two retroreflectors and their longitudinal and lateral movements are utilized to incorporate spatial coherence measurement using this modified Michelson interferometer. In general, one uses Young' double slit interferometer to measure spatial coherence. However, this modified interferometer can be used as an optical setup kept at room temperature outside a cryostat to measure spatio-temporal coherence of a light source placed at cryogenic temperatures. This avoids the added complexities of modulation of interference fringe patterns due to single slit diffraction as well. The process of mixing of spatial and temporal parts of coherences is intrinsic to existing methods for dual measurements. We addressed these issues of spatio-temporal mixing and we introduced a method of 'temporal filtering' in spatial coherence measurements. We also developed a 'curve overlap' method which is used to extend the range of the experimental setup during temporal coherence measurements without compromising the precision. Together, these methods provide major advantages over plane mirror based standard interferometric systems for dual measurements in avoiding systematic errors which lead to inaccuracies especially for light sources with low coherences.

I. Introduction

Optical interferometry has always been prominently used in important experimental investigations. The famous Michelson interferometer for the search of ether, recent gravitational wave detections in LIGO and Young's double slit experiments for validation of wave-particle duality for photons as well as electrons are some of the important examples. Similar applications of optical interferometry are found to be useful in field of biology¹, astronomy², quantum optics³, holography⁴, optical communication⁵, surface topography⁶ etc. Recently, many-body cooperative phenomena in condensed matter physics of light-matter interactions like excitonic lasing⁷⁻¹⁰, polariton lasing¹¹⁻¹⁷ and Bose-Einstein condensation (BEC) of polaritons^{18,19}, excitons²⁰⁻²³ and even photon BEC^{24,25} requires the use of optical interferometry to study coherence of emitted light for rigorous experimental verifications. The light emitted by an extended light source preserves the information of phase coherence over certain time delays and over some area of the source, which are known as temporal and spatial coherence of light, respectively. Measurements of the modulus of first order correlation²⁶ $|g^{(1)}(\Delta r, \Delta \tau)|$ as a function of spatial separation (Δr) and time delay ($\Delta \tau$) can be used to estimate the spatio-temporal coherence of an extended light source. In fact, simultaneous measurements of spatial and temporal coherences can provide new physical insights of emerging many-body condensed matter physics of these light emitting systems^{27,28}. Recently, we also investigated the relation between temporal coherence of emission and auger recombination in III-V semiconductor heterostructure light emitting diode²⁹. Most of these many-body cooperative phenomena also occurs at cryogenic temperatures, which requires a cryostat.

Optical power spectrum³⁰ is connected with the first order correlation function in time through Fourier transform. This can be directly derived from Wiener-Khintchine theorem³¹. Temporal coherence is commonly measured with Michelson and Mach-Zehnder

interferometers. However, there are certain conditions which should be considered while measuring temporal coherence such as the longitudinal spatial coherence³² which can limit the temporal coherence during its measurement. These conditions are discussed in details by Ryabukho et. al³²⁻³⁶ and Abdulhalim^{37,38}. Since we are dealing with interference of light spots sufficiently far from the source, we do not see any significant involvement of longitudinal spatial coherence during the measurement of temporal coherence. For spatial coherence measurement, Young's double slit interferometer³⁹ is typically used. Usually, double slit method yields very low intensity output due to use of narrow slits and it is difficult to use this method when the intensity of light emission is already low. Individual slits also produce their own diffraction patterns which should be filtered/subtracted from double slit interference pattern to correctly measure $|g^{(1)}(\Delta r)|$. Additionally, it is not easy to place double slits with variable slit widths and slit separations within a cryostat in close proximity of the sample for spatial coherence measurements at cryogenic temperatures.

Moreover, using two separate experimental setups for any generalized measurements of first order spatio-temporal correlation $|g^{(1)}(\Delta r, \Delta \tau)|$ can be inconvenient from the point of view of experimentation. Hence, modified Young's interferometer^{34,40,41} and several combinations of Michelson^{27,42-44} and Mach-Zehnder interferometers^{45,33} were used to perform combined measurement of spatial and temporal coherence. A single setup is more convenient to measure both types of coherence but there are instrumentational challenges as interferometry is very sensitive on experimental conditions. One such major challenge is to measure spatial and temporal coherence separately using a single interferometer. The effect of longitudinal spatial coherence in temporal coherence measurement due to properties of the light source has been studied^{32,34,36-38}, but mixing of these coherences due to instrumentational designs is hardly studied. For example, an unwanted spatio-temporal phase always adds up due to tilting of interfering beams. This type of spurious angular

change(s) may occur due to the design and technique of a particular instrument like changing angle of beam for partial overlap, use of one lens for two spatially shifted beams, optical misalignments etc. Some of these temporal phases can add systematic errors during measurement of spatial coherence. In some dual measurement setups reported earlier^{42,45,47}, these unwanted temporal phases are not considered which might lead to additional errors. However, with design modification³³, some of these systematic errors can be reduced but an additional method is required, which assumes that correlation function is not wholly dependent upon the design to minimize the mixing of these phases. Here, we use a technique of 'temporal filtering' method to maximally avoid such unwanted mixing during the measurement of spatial coherence.

It is often required to notice changes in spatio-temporal coherence due to the onset of some physical phenomenon like lasing^{8,14-16}, BEC^{19,48} as mentioned above. There, we require an instrument whose range can be extended to measure these substantial changes. So, during the measurement of temporal coherence, we use a 'curve overlap' method to extend the range of the setup while maintaining its precision. Moreover, this modified Michelson interferometer can offer the technical convenience for such kind of instrumentations where one may not be able to place adjustable double slits for measuring spatial coherence (say) within a cryostat.

We divide this report in four sections. In the section II, we start with a brief introduction of $g^{(1)}(\Delta r, \Delta \tau)$ and its measurement methods. In section III, we first explain the complete experimental details of the instrumentations and then further divide this section into two subsections. Standard operating procedure of Michelson interferometer, data acquisition and analyses methods are described in the subsection on 'Temporal correlation measurement'. The technique of 'curve overlap' and results are also discussed in this subsection. In the second subsection on 'Spatial correlation measurement using the modified Michelson

interferometer', we explain the modifications in acquisition and analyses of Michelson interferometer to measure spatial coherence as well. At the end of this subsection, we discuss the results of this modified setup. Finally, in section IV, we summarize our conclusions.

II. First order correlation function $g^{(1)}(\Delta r, \Delta \tau)$ from optical interference pattern

The first order correlation function between two optical fields is defined as⁴⁹

$$g^{(1)}(r_1, r_2, t_1, t_2) \equiv g^{(1)}(\Delta r, \Delta \tau) = \frac{\langle E(r_1, t_1) E^*(r_2, t_2) \rangle}{\sqrt{\langle |E(r_1, t_1)|^2 \rangle \langle |E(r_2, t_2)|^2 \rangle}} \quad (1)$$

where $E(r_1, t_1)$ and $E(r_2, t_2)$ are two interfering electric fields of light at position r_1 and r_2 at time t_1 and t_2 , respectively. It is also defined in relative terms as $\Delta r = r_1 - r_2$ and $\Delta \tau = t_1 - t_2$. The $\Delta \tau$ is the temporal delay between two interfering fields at one spatial position. In Eq. (1), when space coordinates are kept constant as $r_1 = r_2$, then correlation measured between t_1 and t_2 is called temporal correlation function or $g^{(1)}(\Delta \tau)$. Similarly, when time coordinates are kept constant as $t_1 = t_2$, $g^{(1)}(\Delta r)$ is called spatial correlation function at one point of time. Here Δr is spatial separation between two interfering fields.

The information of spatio-temporal coherence is estimated by measuring the modulus of $g^{(1)}(\Delta r, \Delta \tau)$ function. The $|g^{(1)}(\Delta r, \Delta \tau)|$ is strictly positive quantity ($0 \leq |g^{(1)}(\Delta r, \Delta \tau)| \leq 1$). While using any optical interferometer, the method to measure $|g^{(1)}(\Delta r, \Delta \tau)|$ is to interfere two light fields and analyze their interference pattern. Interference of these light fields forms two dimensional (2D) interference pattern on a screen and one single line/axis (1D) from the pattern is chosen for analysis. This 1D interference pattern can be extracted by modulating^{45,47} the spatio-temporal delays between two optical fields or it can also be directly extracted from the 2D fringe pattern⁵⁰. In either case, a small phase difference between two

fields is introduced to produce the fringe pattern. It is kept much smaller than the operational phase delays introduced while moving the retroreflectors during the actual measurements. This also provides an instrumentational lower bound on $|g^{(1)}(\Delta r, \Delta \tau)|$, which can be measured without mixing temporal and spatial parts. Anyway, all these time delays (or path differences) between two interfering fields must also remain smaller than the coherence time (or lengths) of sources. In this work, we use 2D interference pattern and select one axis to extract fringe pattern for analysis.

The fringe intensity is either fitted with interference formula given below or the simple visibility^{31,49} of fringes is measured to get the value of $|g^{(1)}(\Delta r, \Delta \tau)|$. The 1D interference formula along one axis can be expressed as⁵¹

$$I_{\text{int}}(x) = I_1(x) + I_2(x) + 2|g^{(1)}(\Delta r, \Delta \tau)| \sqrt{I_1(x)I_2(x)} \cos(k_x x - \phi) \quad (2)$$

where x is the 1D coordinate along which the variation of interference pattern is measured on CCD/screen. $I_{\text{int}}(x)$ is intensity due to interference of two fields $E(r_1, t_1)$ and $E(r_2, t_2)$, $I_1(x)$ and $I_2(x)$ are intensities of individual field along the same axis. $k_x x = (\vec{k}_1 - \vec{k}_2) \cdot \vec{x}$, where \vec{k}_1 and \vec{k}_2 are wave vectors of $E(r_1, t_1)$ and $E(r_2, t_2)$, respectively, $(\vec{k}_1 - \vec{k}_2) \cdot \hat{x} = k_x$ and ϕ is a constant phase factor. Once $I_{\text{int}}(x)$, $I_1(x)$ and $I_2(x)$ are known, the $|g^{(1)}(\Delta r, \Delta \tau)|$ can be estimated from the above relation. Here, Δr and $\Delta \tau$ are experimental variables which are set by instrument. The precision of these input variables is instrument dependent.

III. Modified experimental setup to determine temporal and spatial correlation

Schematic diagram of the complete experimental setup is given in Fig. 1(a). We are using a standard Michelson interferometer setup. However, the usual plane mirrors are replaced with two silver coated retroreflector^{52,53} mirrors M_1 and M_2 procured from Holmarc, India and

one CCM1-BS013/M non-polarizing 50:50 beam splitter (BS) from Thorlabs is used. The distances of M_1 and M_2 from center of beam splitter are L_1 and L_2 , respectively. The retroreflectors are also effective in blocking any back-reflection into the light source, which can otherwise create instabilities and affect the coherence of the light source. Double retroreflector design thus prevents any unwanted optical effects such as image flipping (if only one retroreflector is used) and mode hopping, intensity fluctuations, coherence oscillations^{54,55} etc. due to absence of any unwarranted positive feedback from the source during the measurement.

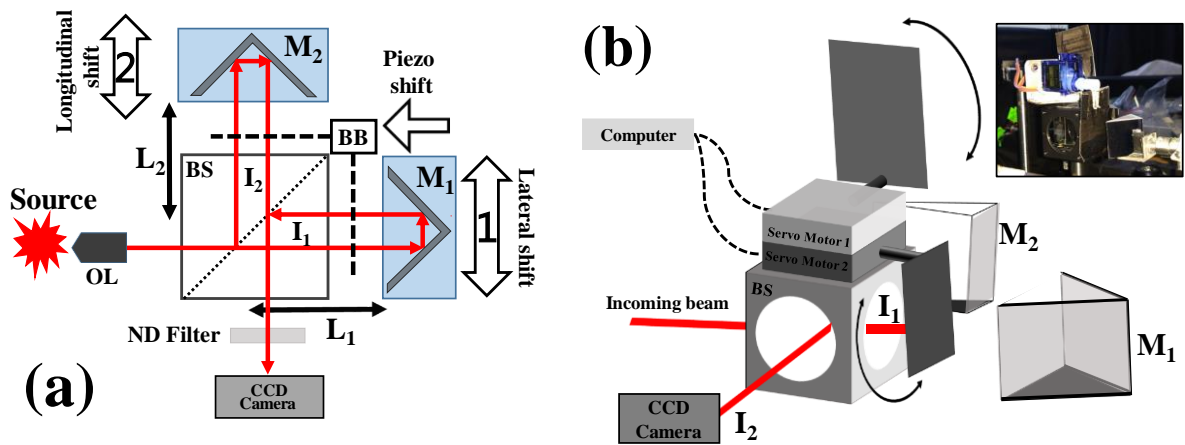


Fig. 1. (a) Schematic diagram of experimental setup based on Michelson interferometer. M_1 and M_2 are two retroreflectors and BS is 50:50 beam splitter. M_1 and M_2 are installed on linear stages to move in the direction shown by arrow 1 and 2, respectively. M_1 is attached to a Piezo actuator which moves in the direction labelled as ‘Piezo shift’. Source is collimated by objective lens (OL) of 10X magnification. The light beam split as I_1 and I_2 are reflected back to generate an interference pattern on the plane of the CCD. The distances of M_1 and M_2 from centre of BS are L_1 and L_2 , respectively. (b) Schematic diagram of beam blocker over BS. In the inset, a real image of BB is shown.

The light source is an AlGaInP based multi-quantum well commercial laser diode HL6358MG (Thorlabs) which emits at a wavelength of 639 nm. The bias to laser diode is given by ITC4001 Controller (Thorlabs). The laser diode has lasing threshold at 30 mA but

whole experiment is done well below lasing threshold, at 1 mA. The reason for using laser diode in a non-lasing mode is because we are interested in making an experimental setup which can be used for measuring small and variable coherence of a light source. The source is collimated by using a 10X objective lens. M_1 is attached to a piezo actuator PAS005 (Thorlabs). Piezo can move up to $\sim 16 \mu\text{m}$. The direction of piezo displacement is shown by arrow labelled as 'Piezo shift' in Fig. 1(a). The Piezo and M_1 combination is fitted on a kinematic alignment mount for beam alignment. This kinematic mount is installed on a linear stage which moves in the direction indicated by arrow 1 (lateral shift). This stage has precision of $10 \mu\text{m}$ and it can move up to 25 mm. Similarly, the other retroreflector M_2 is also fitted with a similar kinematic mount (without Piezo actuator) on a linear stage. This stage of M_2 moves in direction shown by arrow 2. We call it as longitudinal shift. These manual stages are moved by stepper motors and are remotely controlled using a computer.

Beams reflected from M_1 and M_2 , indicated as beam I_1 and I_2 , are made to interfere at the CCD camera of BC106N-VIS/M beam profiler (Thorlabs). The sensor of CCD has 1360×1024 pixels and sensor area is $\sim 8.77 \times 6.60 \text{ mm}^2$. The distance on CCD sensor are recorded in terms of pixel number. These pixel numbers are converted to distance (μm or mm) and are defined in X-Y coordinates (CCD sensor coordinates). In front of the CCD camera, we use neutral density (ND) filters from Newport to reduce the light intensity by 0.3 dB to 4 dB. This is to protect camera sensor from any intense light and subsequent overloads. Over the beam splitter, we have installed a custom made beam blocker (BB) which use two servo motors and two opaque sheets, as shown in Fig. 1(b), to block either arm of the interferometer. It blocks I_1 beam while letting I_2 to pass and vice versa to measure I_1 and I_2 separately. In the inset of the same figure, the real image of beam blocker is shown. This whole setup (except the light source and CCD camera) is assembled on a single optical breadboard ($25\text{cm} \times$

25cm). After initial alignment, we can easily relocate this portable setup to use it in different experiments. Initial alignment of whole setup is done with a He-Ne Gas laser.

A. Temporal correlation measurement

The lateral shift of M_1 can move I_1 beam horizontally on the screen of CCD. For measurement of temporal correlation, in Fig. 1(a), the linear stage of M_1 is locked at a position in lateral direction such that I_1 and I_2 beams are completely overlapping with each other. Although, M_1 is locked for any lateral shift, but piezo actuator attached with M_1 moves in the direction shown in Fig. 1(a). Hence, piezo movement of M_1 is to produce fine temporal delay while longitudinal movement of M_2 is to produce coarse temporal delays between I_1 and I_2 beams. The temporal delay $\Delta\tau = 2*(L_2 - L_1)/c$ where $(L_2 - L_1)$ is the length difference between two arms of the interferometer and c is speed of light. Linear stage of M_2 produces $\Delta\tau \sim 66$ fs when moved by $10 \mu\text{m}$. Piezo steps are not constant but change quadratically as a function of piezo voltage. It can cover total $\Delta\tau \sim 108$ fs in 40 steps.

1. Data Acquisition Method

We collect 2D images of I_1 , I_2 and I_{int} along with camera parameters such as gain, exposure-time, saturation and sensor temperature for each image. The camera is used in auto-exposure mode to automatically maintain the optimum values of gain and exposure time depending upon the light intensity. Moreover, we used LabView based data acquisition algorithm to select images which have approximately similar values of these camera parameters. Detailed flow-chart for data acquisition is shown in Fig. 2. For initial alignment, we adjust M_1 and M_2 stages and kinematic mounts for total overlap of I_1 and I_2 beam spots on CCD. Then, we save image of I_1 by blocking the I_2 beam. We mark the position of I_1 spot

by using four cursor lines on the CCD output screen. Then, we block I_1 while opening I_2 and adjust the spot position of I_2 beam according to the set cursor lines to ensure the total beam overlap. We save the image of I_2 after making sure that both beam spots are properly overlapping. For saving the image of I_{int} , both the paths are kept open. Images of I_{int} are saved

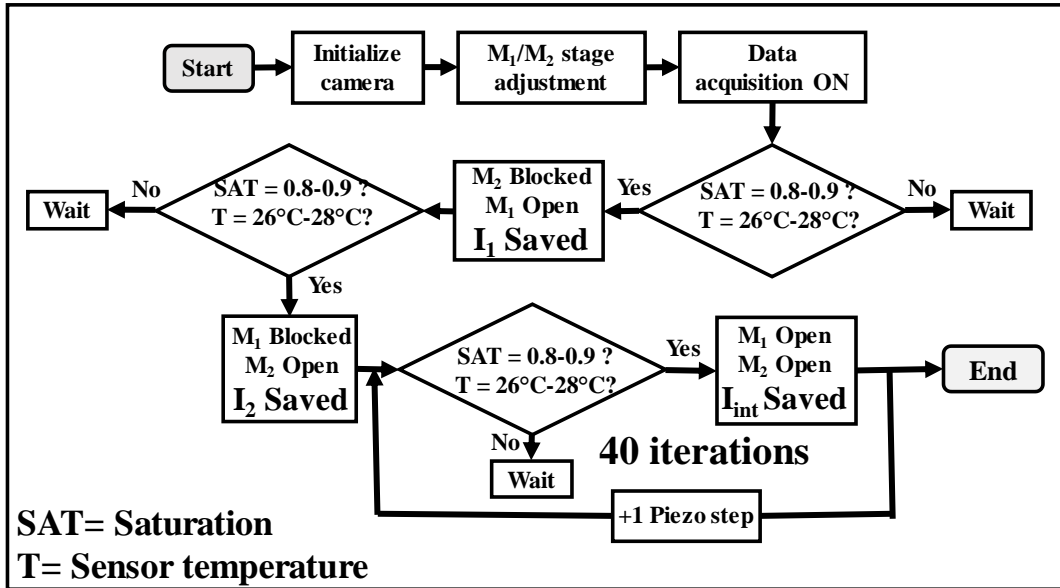


Fig. 2. Flow-chart of data acquisition method used in the experiment. Saturation value (SAT), and sensor temperature (T) of camera are kept in narrow range while saving 2D images to minimise the impact of camera parameters. Using beam blocker, I_1 and I_2 are saved by blocking M_2 and M_1 , respectively. For each step of stage M_1 (or M_2 for the case of spatial correlation measurement), I_1 and I_2 are saved and images of I_{int} are also saved at each of the 40 steps of the piezo.

at each of the 40 steps of the piezo movement during a single run. For the coarse temporal delay, the linear stage of M_2 is set to the next step and piezo steps are again repeated. Since total fine delay is almost twice the coarse delay, some portion of data is repeated at each linear stage step.

2. Data Analysis Method

The collected 2D images are saved as 2D arrays. The scaling is done by dividing these 2D-arrays by their corresponding gain and exposure time values. From the 2D image of I_{int} , one axis is chosen to extract the 1D data. One such image is given in Fig. 3(a) and chosen axis is indicated by σ -axis at the centre of I_{int} image shown by black dashed line. X-Y axis are CCD sensor coordinates along the horizontal and vertical directions. The choice of σ -axis as perpendicular to X-axis is mainly to maintain the similarity with measurements of spatial coherence along the X-axis itself. The intensity values over this axis are extracted from images of I_{int} , I_1 and I_2 as $I_{int}(\sigma)$, $I_1(\sigma)$ and $I_2(\sigma)$. We take 10 pixels on either side of σ -axis and average these intensities. This averaging is done to avoid any pixel related errors. Estimated values of $I_{int}(\sigma)$, $I_1(\sigma)$ and $I_2(\sigma)$ are shown separately in Fig. 3(b).

To calculate $|g^{(1)}(\Delta\tau)|$ from these data, we rearrange Eq. (2) and replace the 'x' coordinates with our chosen σ -coordinates to get the cosine function as -

$$\frac{I_{int}(\sigma)-I_1(\sigma)-I_2(\sigma)}{2\sqrt{I_1(\sigma)I_2(\sigma)}} = |g^{(1)}(\Delta\tau)| \cos(k_\sigma \cdot \sigma - \phi) \equiv S(\sigma) \quad (3)$$

Here, $S(\sigma)$ is acquired by using intensities of $I_{int}(\sigma)$, $I_1(\sigma)$ and $I_2(\sigma)$ in Eq. (3). If all intensities are corrected for the above mentioned scaling, $S(\sigma)$ should mimic the cosine function and the amplitude of this function should be equal to $|g^{(1)}(\Delta\tau)|$. The $S(\sigma)$, estimated for $I_{int}(\sigma)$, $I_1(\sigma)$ and $I_2(\sigma)$ of Fig. 3(b), is shown in Fig. 3(c). As mentioned in section II, $|g^{(1)}(\Delta\tau)|$ is strictly positive ($0 \leq |g^{(1)}(\Delta\tau)| \leq 1$). Also, dark currents of CCD and other electronics can affect the estimate of $S(\sigma)$. Therefore, instead of fitting $S(\sigma)$ with a simple cosine function, we modify the fitting function as

$$\text{Fitting function of } S(\sigma) = S_0 + \exp(b) \cos\left(\frac{\sigma - \sigma_0}{d}\right) \quad (4)$$

where $|g^{(1)}(\Delta\tau)| = \exp(b)$ fulfills the condition of $|g^{(1)}(\Delta\tau)| > 0$ and S_0 is an offset which shows

effect of dark currents or systematic errors in calculation of $|g^{(1)}(\Delta\tau)|$. The d and σ_0 depend upon values of k_σ and ϕ . We select the central section from $S(\sigma)$ to include at least 2-3 oscillations for cosine fitting shown as red dashed rectangle in Fig. 3(c).

In Fig. 3(a), from CCD sensor coordinate axis $X \sim 3.87$ mm to $X \sim 6.13$ mm (as shown by red dashed lines), different σ -axis with separation of ~ 0.06 mm (10 pixels) are chosen to estimate $|g^{(1)}(\Delta\tau)|$. Here, we do not take the average over 21 adjacent pixels. These $|g^{(1)}(\Delta\tau)|$

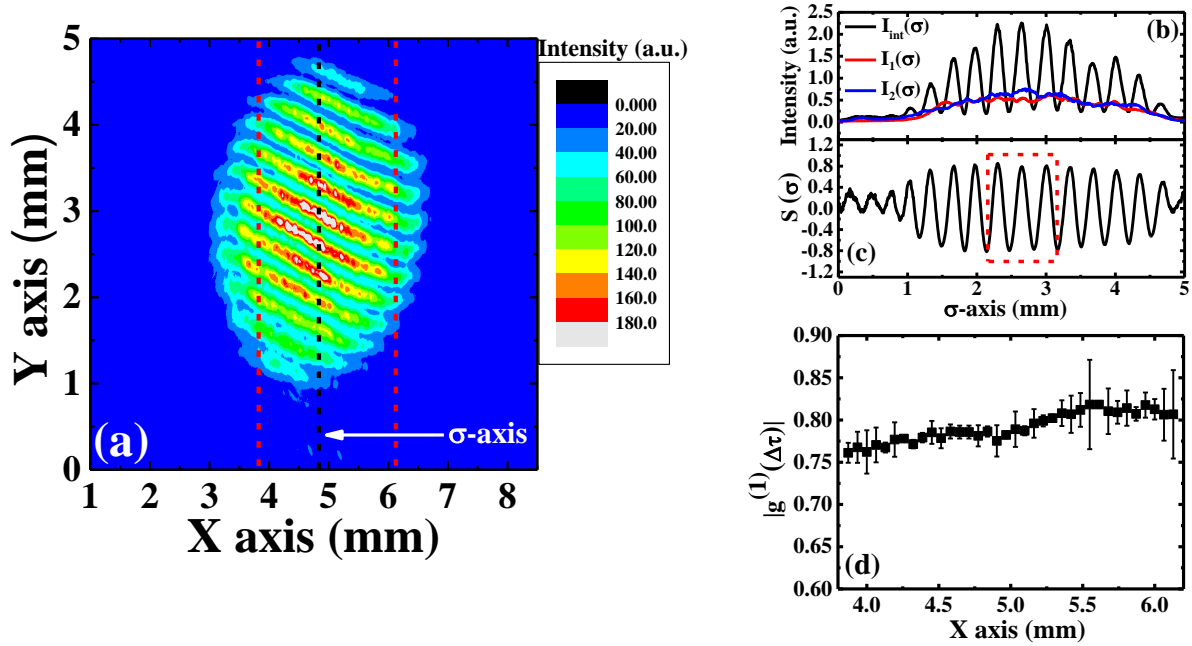


Fig. 3. (a) Interference image due to complete overlap of I_1 and I_2 beams. X-Y are camera sensor coordinates. Temporal correlation measurements are done maintaining this overlap condition. The σ -axis is in the centre of interference pattern indicated by black dashed line. (b) $I_1(\sigma)$, $I_2(\sigma)$ and $I_{int}(\sigma)$ are extracted from interference image along σ -axis. (c) $S(\sigma)$ is calculated using Eq. (3). Different σ -axes are chosen from sensor coordinate $X \sim 3.87$ mm to $X \sim 6.13$ mm indicated by red dashed line on (a). The value of $|g^{(1)}(\Delta\tau)|$ is calculated along these σ -axes and are plotted against sensor X coordinates in (d). Error bars are offset S_0 from Eq. (4).

are plotted in Fig. 3(d) with offset S_0 as error bar for comparisons. It shows that S_0 are small compared to $|g^{(1)}(\Delta\tau)|$ values. Most importantly, it is seen that small variations in the selection of σ -axis do not affect the results. The mean value of all the $|g^{(1)}(\Delta\tau)|$ is 0.79 and standard

error is 0.01. Hence, the methods adopted for data acquisition and analyses are robust against such small displacements of σ -axis.

3. Discussion of Experimental results on Temporal Coherence Measurement

To calculate $|g^{(1)}(\Delta\tau)|$, we make two beams to overlap completely reducing $\Delta r \sim 0$ mm as mentioned in section III.A.1. We set linear stage of M_2 at a starting point τ_0 and then another 40 piezo steps are taken in the direction of 'piezo shift' (see Fig. 1(a)). Then, M_2 stage is moved by one step (~ 66 fs) to the point $\tau_0 + 66$ fs and again 40 piezo steps are taken. This way, the piezo and linear stage can provide fine and coarse delay ($\Delta\tau$), respectively. In Fig. 4(a), multiple curves are shown and each individual curve is $|g^{(1)}(\Delta\tau)|$ calculated for piezo steps while different curves are for steps of M_2 stage. The temporal position of M_2 stage is indicated by $[\tau_0 + 1 \times 66]$ fs, $[\tau_0 + 2 \times 66]$ fs etc. As we already mentioned, step of M_2 stage is of ~ 66 fs and 40 steps of piezo covers ~ 108 fs. Hence we see significant overlapping between adjacent curves of $|g^{(1)}(\Delta\tau)|$. We translate these individual curves to overlap into a single curve as shown in inset of Fig. 4(a). The maximum overlapping condition is decided when Δg is minimum for overlapping portion of two curves. This Δg is defined as,

$$\Delta g = \frac{\sum_i \{(g_n^{(1)})_i(\Delta\tau) - (g_{n+1}^{(1)})_i(\Delta\tau \pm t)\}}{\sum_i} \quad (5)$$

where i = number of overlapping point in curve. $(g_{n+1}^{(1)})_i$ are points of $(n+1)^{\text{th}}$ curve of M_2 stage which overlap with adjacent $(n)^{\text{th}}$ curve. The $(n+1)^{\text{th}}$ curve is translated in $\Delta\tau$ by the unit of $t = N \times (\text{minimum step of piezo})$ where $N = 1, 2, 3, \dots$. The overlapped curves are then stitched together to produce single curve of $|g^{(1)}(\Delta\tau)|$ as shown in Fig. 4(b). The main benefit of the curve overlap method is that it extends the range of measurement while retaining the precision. We mentioned few physical phenomena in section I where coherence of the source

changes and this curve overlap method can be very helpful to measure those changes in coherence. Moreover, good overlap also indicates good reproducibility and reliability of data. The error bars used in the plot are the 95% confidence interval (CI). The CI is calculated by multiplying standard error to student-t inverse cumulative distribution function. The standard error is calculated from covariance matrix which is generated for the fitting parameters of Eq. (4). The S_0 values which represent the offset due to dark currents of CCD are smaller in comparison with the 95% CI. The instrumental errors/uncertainties in $I_{\text{int}}(\sigma)$, $I_1(\sigma)$ and $I_2(\sigma)$ due to CCD propagate to the error of estimated $|g^{(1)}(\Delta\tau)|$ (see Eq. (3)). This is also small in comparison with the 95% CI. Therefore, only the CI is used as error bars. Each curve overlaps

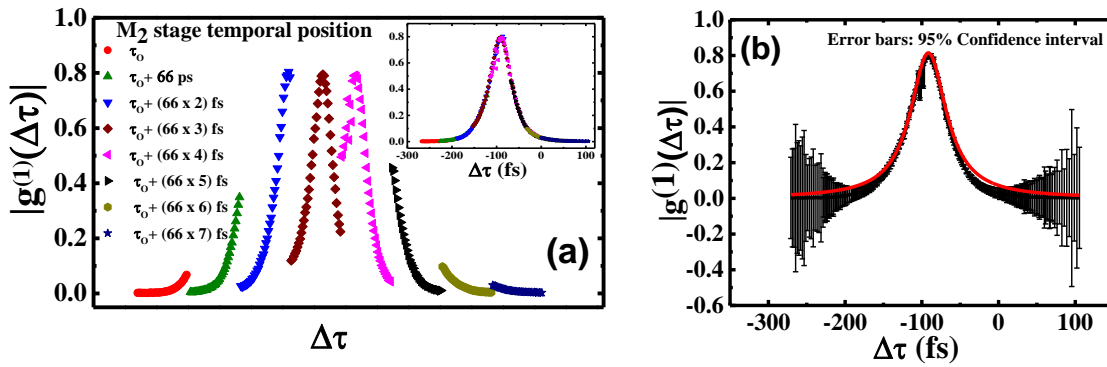


Fig. 4. (a) shows the estimated $|g^{(1)}(\Delta\tau)|$ plotted against fine motion of piezo ($\Delta\tau$) at different M_2 stage temporal position. Plots of different M_2 stage are manually segregated along $\Delta\tau$ axis for clarity. Therefore, scale markers along $\Delta\tau$ are not given. M_2 stage has coarse temporal delay of $\Delta\tau \approx 66$ fs and total piezo temporal delay is ~ 108 fs. Therefore, there are significant overlapping between adjacent curves. Inset of (a) shows the overlapped curve by translating individual curves on $\Delta\tau$ axis. (b) Overlapped curves are then stitched to a single curve and fitted with Lorentzian function. Fitting is shown as red line. Error bars are of 95% confidence interval.

with two immediate adjacent curves on either side by $\sim 60\%$ and two more adjacent curves by $\sim 20\%$. Any misaligned overlap would have suggested that either the source is not stable or there are changes due to movement of M_2 stage. However, we see reasonably good extent

of curve overlaps in inset of Fig. 4(a). This indicate that data is reproducible even after movements of linear stage M_2 and the beam alignment is maintained to fulfil the condition of total beam overlap. These matching overlaps further validate our instrumentation and the method of analyses as mentioned above. The full curve of $|g^{(1)}(\Delta\tau)|$ is then fitted with Lorentzian function,

$$|g^{(1)}(\Delta\tau)| = g_0 + \frac{2(A)}{\pi} \left(\frac{w}{4(\Delta\tau - \Delta\tau_{\text{center}})^2 + w^2} \right) \quad (6)$$

where $g_0 (\geq 0)$ is offset, w is FWHM, A is area and $\Delta\tau_{\text{center}}$ is centre of curve on $\Delta\tau$ axis. g_0 is 0.0, $\Delta\tau_{\text{center}}$ is -91 fs, A is 73 fs² and FWHM is 57 fs. R^2 value of fitting is 0.979. The approximated coherence time (τ_c) of the source is FWHM the curve of $|g^{(1)}(\Delta\tau)|$. The error in FWHM due to fitting is 1 fs. The highest step size of our piezo is ~3 fs. So this step size is used as scale of error in the measurement of $\Delta\tau$. Therefore, the estimated coherence time (τ_c) is 57 ± 3 fs. We also calculate (95% CI of $|g^{(1)}(\Delta\tau)| / |g^{(1)}(\Delta\tau)|$ to be < 0.1 for values of $|g^{(1)}(\Delta\tau)| > 0.17$. The same value is < 0.5 for $|g^{(1)}(\Delta\tau)| > 0.05$. We also calculated the Fourier transform³⁰ of the measured optical power spectra of the source and then estimated the coherence time as ~62 fs from its FWHM using Wiener-Khintchine theorem³¹. Therefore, it shows that two independent measurements estimate approximately similar values of τ_c . This establish that our Michelson interferometer is working properly.

B. Spatial correlation measurement using the modified Michelson interferometer

In the modified Michelson inteferometer, when I_1 and I_2 beams partially overlap on CCD plane, the resulting interference contains the information about spatial correlation. To understand this, we draw the schematic of the original light beam's cross sectional image before it passes through beam splitter in Fig. 5 (left). The different dotted and dashed lines

indicate different parts of the beam spot and identical lines among these are separated by distance Δr . The schematics of the reflected beams from M_1 and M_2 on CCD are shown in Fig. 5 (right). If the separation between two beams (I_1 and I_2) is Δr , the identical lines will be in complete overlap. The interference generated by this partial overlap (Δr) can be used to measure spatial coherence if $\Delta\tau \sim 0$.

In previous experiments, the partial overlap is achieved by changing the reflection angle of one of the mirrors⁴⁵ of interferometer or by spatially inverting one of the beams^{27,28,42,44,56} with only one retroreflector. The change in reflection angle and merging of spatially shifted beams also change the angle between overlapping beams. This angular deviation leads to unwanted temporal phase difference. To avoid this, linear deviation of the beam instead of angular deviation is used to achieve partial overlap⁴⁷ while measuring spatial coherence. In Fig. 1(a), I_1 beam is shifted by laterally shifting the linear stage of M_1 in direction as indicated

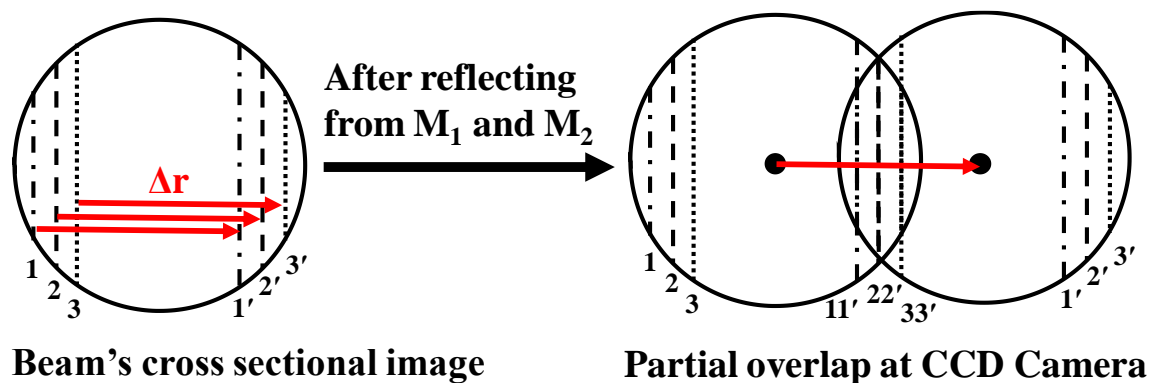


Fig. 5. (Left) Schematic cross-sectional image of beam originating from objective lens before entering to beam splitter. Identical dotted and dashed lines (1 and 1', 2 and 2', 3 and 3') are Δr distance apart in the same beam. (Right) Partially overlapping image of I_1 and I_2 after reflecting back from M_1 and M_2 . The beams are Δr distance apart and identical dotted and dashed lines overlap. The resulting interference pattern due to this partial overlap can be used to measure spatial coherence, if $\Delta\tau \sim 0$. This ideal schematic, however, does not include the small phase difference introduced to obtain the fringe pattern in the first place.

by arrow 1. M_2 is locked in position of $\Delta\tau=0$. The lateral shift of M_1 shifts the I_1 beam without any angular deviation, hence, it prevents any additional $\Delta\tau$. We use CCD sensor coordinates to measure the lateral shift of I_1 by noticing the shift in specific marker on beam when M_1 is being shifted. The pixel size of the CCD sensor is $6.45 \mu\text{m}$, which limits the spatial resolution.

In Fig. 6(a), 2D image of the interference pattern I_{int} is shown for partial separation of I_1 and I_2 by $\Delta r \sim 2.8 \text{ mm}$ on CCD sensor coordinates. The σ -axis is chosen at the middle of fringe pattern and perpendicular to the direction of spatial translation along X , which is parallel to the lateral shift of M_1 along the horizontal plane. The measured $I_{\text{int}}(\sigma)$, $I_1(\sigma)$, $I_2(\sigma)$ are plotted

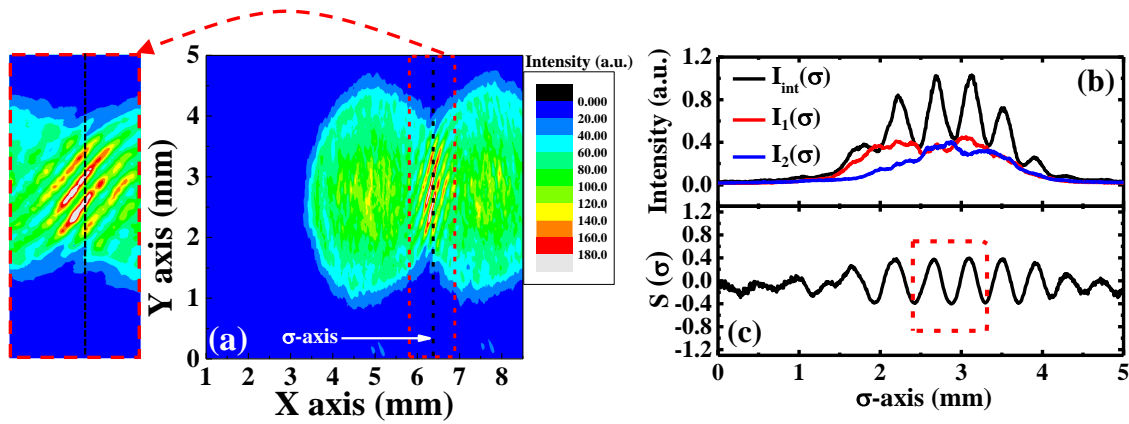


Fig. 6. (a) Interfere image due to partial overlap of I_1 and I_2 beams. Beams are separated by $\sim 2.8 \text{ mm}$ on CCD sensor coordinates. The σ -axis is in the centre of interference pattern indicated by black dashed line. Magnified image of interference pattern is shown in red dashed lined box (left). (b) $I_1(\sigma)$, $I_2(\sigma)$ and $I_{\text{int}}(\sigma)$ are extracted from interference image along σ -axis. (c) $S(\sigma)$ is estimated using Eq. (3).

in Fig. 6(b). The $S(\sigma)$ is calculated from these intensities using Eq. (3) and $S(\sigma)$ shows a clear cosine pattern in Fig. 6(c). The central portion of $S(\sigma)$ is taken for fitting with Eq. (4) as shown by red dashed rectangle and the amplitude of this cosine function is estimate of $|g^{(1)}(\Delta r)|$. After the partial overlap, one can also use visibility to measure $|g^{(1)}(\Delta r)|$ as,

$$\text{Visibility} = \frac{I_{\max} - I_{\min}}{I_{\max} + I_{\min}} = 2|g^{(1)}(\Delta r)| \frac{\sqrt{I_1(\sigma) I_2(\sigma)}}{[I_1(\sigma) + I_2(\sigma)]} \quad (7)$$

where I_{\max} and I_{\min} are successive maximum and minimum intensity of interference pattern ($I_{\text{int}}(\sigma)$) on central portion of σ -axis, $I_1(\sigma)$ and $I_2(\sigma)$ are intensity of individual beam for the same portion. This formula, however, requires the strict condition of $I_1(\sigma) = I_2(\sigma)$ for visibility = $|g^{(1)}(\Delta r)|$. However, the light beam may not be symmetric in intensity around the center for many sources, therefore $I_1(\sigma)$ and $I_2(\sigma)$ can have different intensities. Therefore, we avoid using visibility as a measure of $|g^{(1)}(\Delta r)|$ and individually take $I_1(\sigma)$ and $I_2(\sigma)$. We use Eq. (3) and (4) to get $|g^{(1)}(\Delta r)|$. The detailed data acquisition method is already given in section III.A.1 where instead of total overlap, we only partially overlap light beams to introduce Δr .

1. Data Acquisition, Analysis and Results on Spatial Coherence Measurement

As discussed above, to eliminate the involvement of unavoidable temporal phase, we used the lateral shift of M_1 . However, there can be other source of unwanted temporal phase as well which we discussed in section I. We use a technique called ‘temporal filtering’ in spatial coherence measurement filter out any temporal phase. Here, we use piezo to make temporal correlation scan for every step of M_1 . At every beam separation (Δr), piezo takes 40 temporal steps to measure $|g^{(1)}(\Delta r, \Delta \tau)|$. The Δr is introduced by lateral shift of M_1 and $\Delta \tau$ is due to piezo shift. These $|g^{(1)}(\Delta r, \Delta \tau)|$ at different Δr values are plotted in Fig. 7(a). The maximum value of $|g^{(1)}(\Delta r, \Delta \tau)|$ of every curve indicates the position of where $\Delta \tau = 0$. By picking these points $|g^{(1)}(\Delta r, \Delta \tau = 0)|$ the involvement of any temporal phase is eliminated. $|g^{(1)}(\Delta r, \Delta \tau = 0)|$ are plotted against Δr in Fig. 7(b). This way, we are able to filter contributions of $\Delta \tau$ in spatial coherence measurement and $|g^{(1)}(\Delta r)|$ is estimated. The curve of $|g^{(1)}(\Delta r)|$ is fitted with Lorentzian function as given in Eq. (6) where $\Delta \tau$ and $\Delta \tau_{\text{center}}$ is replaced by Δr and Δr_{center} . R^2 value of

fitting is 0.994. g_0 is 0.2, Δr_{center} is 0.01 and A is 3.8 mm^2 . FWHM is 3.8 mm with standard error of fitting $\sim 0.2 \text{ mm}$. Here, the standard error of fitting is greater than the instrumental precision of Δr , hence it is being used as uncertainty of the estimated FWHM. The FWHM length can be called as the spatial separation on beam spot up to which phase correlation is significant. Since we are using magnification of 10X, on the emitting surface of source, this length is $380 \pm 20 \text{ }\mu\text{m}$. This is called ‘spatial coherence length’ (Δr_c) on the surface of emission.

The reason why ‘spatial filtering’ is not used during temporal coherence measurement is because any significant spatial shift of two beam spots can be detected on CCD screen. We explained in section III.A.1 that four cursor lines are used to mark the position of individual

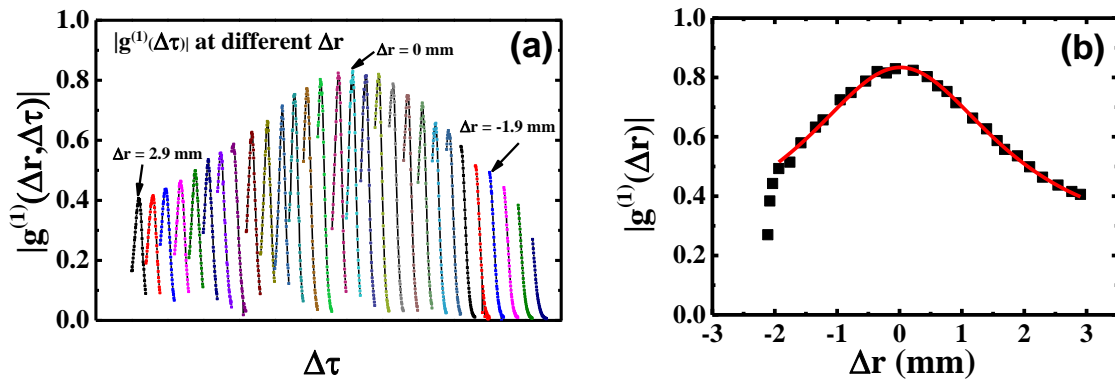


Fig. 7. (a) shows the calculated $|g^{(1)}(\Delta\tau)|$ plotted against fine motion of piezo ($\Delta\tau$) for different spatial separation (Δr) of l_1 and l_2 . The l_1 beam shifts laterally from $\Delta r = 2.9 \text{ mm}$ to $\Delta r = -2.0 \text{ mm}$ with respect to l_2 beam. At each Δr , the individual curve shows $|g^{(1)}(\Delta\tau)|$ plotted against fine $\Delta\tau$ variations of the piezo actuator. The maxima of these curves is $|g^{(1)}(\Delta r, \Delta\tau=0)|$. For each plot with different Δr , the $\Delta\tau$ is varied by $\sim 108 \text{ fs}$ and plots of different Δr are manually segregated along $\Delta\tau$ axis for clarity. Therefore, scale markers are not given along $\Delta\tau$ in this plot. (b) shows $|g^{(1)}(\Delta r, \Delta\tau=0)|$ plotted against Δr as $|g^{(1)}(\Delta r)|$. The curve is fitted with Lorentzian function and indicated by red line.

beam spot to avoid any spatial shift. On the other hand, if additional temporal phase is introduced through instrumentations, it cannot be easily detected from the beam overlap.

Therefore, such effect of any additional unwanted temporal phase must be corrected using temporal filtering method described above.

IV. Conclusion

We have modified a Michelson interferometer which can be used simultaneously for dual measurements of temporal and spatial coherence of a light source. This is specifically useful in cases where installations of double slits with variable widths and slit separations are not possible in close proximity of the source itself. Because of unwanted mixing of temporal and spatial part of coherences, it becomes difficult to estimate the nature of coherence of extended light sources. So, here we present a technique for dual measurement of coherence using a single experimental setup where we use lateral degree of freedom of one of the retroreflector to include spatial coherence measurement. We also vary the temporal delay to find the maximum of first order correlation function to estimate spatial coherence by filtering out additional temporal phase. We call this method as 'temporal filtering' in spatial coherence measurements. Similarly, another technique of 'curve overlap' was developed to extend the range of this instrument while retaining the precision. We provided detailed error analyses of these correlation measurements in section III.A.3. Therefore, this new interferometric technique can become more versatile for exploring the underlying physics of spatio-temporal coherence of an extended light source placed within a cryostat. Similar methods can be extended for measuring spatio-temporal coherences of distant light sources as well.

Acknowledgements

MKS is thankful to IISER-Pune for Integrated PhD Fellowship. SD acknowledges the Department of Science and Technology (DST), India (Grants # DIA/2018/000029, SR/NM/TP13/2016, CRG/2019/000412) for support. We appreciate our discussions with Dr. Sunil Nair and Dr. Shivprasad Patil of IISER-Pune.

Data Availability

The data that support the findings of this study are available from the corresponding author upon reasonable request(s).

References

- ¹ D.D. Nolte, *Optical Interferometry for Biology and Medicine*, 1st ed. (Springer, New York, NY, 2012).
- ² A. Labeyrie, S.G. Lipson, and P. Nisenson, *An Introduction to Optical Stellar Interferometry* (Cambridge University Press, Cambridge, 2006).
- ³ M. Fox, *Quantum Optics: An Introduction* (Oxford University Press, 2006).
- ⁴ P.K. Rastogi, editor, *Holographic Interferometry* (Springer Berlin Heidelberg, Berlin, Heidelberg, 1994).
- ⁵ R.P. Dionisio, in *Interferom. Appl. All-Optical Commun. Networks Opt. Interferom.* (InTech, London, 2017).
- ⁶ R. Leach, *Optical Measurement of Surface Topography* (Springer Berlin Heidelberg, Berlin, Heidelberg, 2011).
- ⁷ R. Matsuzaki, H. Soma, K. Fukuoka, K. Kodama, A. Asahara, T. Suemoto, Y. Adachi,

and T. Uchino, Phys. Rev. B **96**, (2017).

⁸ Z.K. Tang, M. Kawasaki, A. Ohtomo, H. Koinuma, and Y. Segawa, J. Cryst. Growth **287**, 169 (2006).

⁹ Y.Y. Lai, Y.H. Chou, Y.P. Lan, T.C. Lu, S.C. Wang, and Y. Yamamoto, Sci. Rep. **6**, 1 (2016).

¹⁰ T. Shih, E. Mazur, J.P. Richters, J. Gutowski, and T. Voss, J. Appl. Phys. **109**, (2011).

¹¹ G.C. La Rocca, Nat. Photonics **4**, 343 (2010).

¹² S. Christopoulos, G.B.H. Von Högersthal, A.J.D. Grundy, P.G. Lagoudakis, A. V. Kavokin, J.J. Baumberg, G. Christmann, R. Butté, E. Feltn, J.F. Carlin, and N. Grandjean, Phys. Rev. Lett. **98**, 1 (2007).

¹³ P. Bhattacharya, T. Frost, S. Deshpande, M.Z. Baten, A. Hazari, and A. Das, Phys. Rev. Lett. **112**, 29 (2014).

¹⁴ C. Schneider, A. Rahimi-Iman, N.Y. Kim, J. Fischer, I.G. Savenko, M. Amthor, M. Lermer, A. Wolf, L. Worschech, V.D. Kulakovskii, I.A. Shelykh, M. Kamp, S. Reitzenstein, A. Forchel, Y. Yamamoto, and S. Höfling, Nature **497**, 348 (2013).

¹⁵ D. Bajoni, P. Senellart, E. Wertz, I. Sagnes, A. Miard, A. Lemaître, and J. Bloch, Phys. Rev. Lett. **100**, 1 (2008).

¹⁶ Y. V. Kartashov and D. V. Skryabin, Phys. Rev. Lett. **122**, 83902 (2019).

¹⁷ A. Imamoglu, R.J. Ram, S. Pau, and Y. Yamamoto, Phys. Rev. A - At. Mol. Opt. Phys. **53**, 4250 (1996).

¹⁸ T. Byrnes, N.Y. Kim, and Y. Yamamoto, Nat. Phys. **10**, 803 (2014).

¹⁹ Y. Sun, P. Wen, Y. Yoon, G. Liu, M. Steger, L.N. Pfeiffer, K. West, D.W. Snoke, and

K.A. Nelson, Phys. Rev. Lett. **118**, 1 (2017).

²⁰ J.P. Eisenstein and M. A.H, Nature **432**, 691 (2004).

²¹ J.M. Blatt, K.W. Böer, and W. Brandt, Phys. Rev. **126**, 1691 (1962).

²² D.W. Snoke, J.P. Wolfe, and A. Mysyrowicz, Phys. Rev. B **41**, 11171 (1990).

²³ L. V. Butov, C.W. Lai, A.L. Ivanov, A.C. Gossard, and D.S. Chemla, Nature **417**, 47 (2002).

²⁴ J. Klaers, J. Schmitt, F. Vewinger, and M. Weitz, Nature **468**, 545 (2010).

²⁵ C. Kurtscheid, D. Dung, E. Busley, F. Vewinger, A. Rosch, and M. Weitz, Science (80-.). **366**, 894 (2019).

²⁶ Dylan Trotsek, J. Chem. Inf. Model. **110**, 1689 (2017).

²⁷ G. Roumpos, M.D. Fraser, A. Löffler, S. Höfling, A. Forchel, and Y. Yamamoto, Nat. Phys. **7**, 129 (2011).

²⁸ K.G. Lagoudakis, T. Ostatnický, A. V. Kavokin, Y.G. Rubo, R. André, and B. Deveaud-Plédran, Science (80-.). **326**, 974 (2009).

²⁹ M.K. Singh, A. Bhunia, M. Al Huwayz, Y.G. Gobato, M. Henini, and S. Datta, J. Phys. D. Appl. Phys. **52**, (2019).

³⁰ C. Akcay, P. Parrein, and J.P. Rolland, Appl. Opt. **41**, 5256 (2002).

³¹ H. Eugene, *Optics*, 4th ed. (Addison Wesley MA, 2002).

³² V.P. Ryabukho, D. V. Lyakin, and V. V. Lychagov, Opt. Spectrosc. (English Transl. Opt. i Spektrosk. **107**, 282 (2009).

³³ V.P. Ryabukho, D. V. Lyakin, and M.I. Lobachev, Tech. Phys. Lett. **30**, 64 (2004).

- ³⁴ V.P. Ryabukho, A.L. Kal'yanov, D. V. Lyakin, and V. V. Lychagov, *Opt. Spectrosc.* (English Transl. *Opt. i Spektrosk.* **108**, 979 (2010)).
- ³⁵ V.P. Ryabukho, D. V. Lyakin, and M.I. Lobachev, *Opt. Spectrosc.* (English Transl. *Opt. i Spektrosk.* **97**, 299 (2004)).
- ³⁶ V.P. Ryabukho, D. V. Lyakin, and V. V. Lychagov, *Opt. Spectrosc.* (English Transl. *Opt. i Spektrosk.* **102**, 918 (2007)).
- ³⁷ I. Abdulhalim, *J. Opt. A Pure Appl. Opt.* **8**, 952 (2006).
- ³⁸ I. Abdulhalim, *Ann. Phys.* **524**, 787 (2012).
- ³⁹ H. Deng, G.S. Solomon, R. Hey, K.H. Ploog, and Y. Yamamoto, *Phys. Rev. Lett.* **99**, 1 (2007).
- ⁴⁰ N. Takai, H. Amber, and T. Asakura, *Opt. Commun.* **60**, 123 (1986).
- ⁴¹ E. Wertz, L. Ferrier, D.D. Solnyshkov, R. Johne, D. Sanvitto, A. Lemaître, I. Sagnes, R. Grousson, A. V. Kavokin, P. Senellart, G. Malpuech, and J. Bloch, *Nat. Phys.* **6**, 860 (2010).
- ⁴² J. Kasprzak, M. Richard, S. Kundermann, A. Baas, P. Jeambrun, J.M.J. Keeling, F.M. Marchetti, M.H. Szymńska, R. André, J.L. Staehli, V. Savona, P.B. Littlewood, B. Deveaud, and L.S. Dang, *Nature* **443**, 409 (2006).
- ⁴³ F. Manni, K.G. Lagoudakis, B. Pietka, L. Fontanesi, M. Wouters, V. Savona, R. André, and B. Deveaud-Plédran, *Phys. Rev. Lett.* **106**, 1 (2011).
- ⁴⁴ K.S. Daskalakis, S.A. Maier, R. Murray, and S. Kéna-Cohen, *Nat. Mater.* **13**, 271 (2014).
- ⁴⁵ J. Marelic, L.F. Zajiczek, H.J. Hesten, K.H. Leung, E. Yx Ong, F. Mintert, and R.A. Nyman, *New J. Phys.* **18**, 1 (2016).
- ⁴⁶ A. Efimov, *Opt. Express* **22**, 15577 (2014).

- ⁴⁷ A. Efimov, *Opt. Lett.* **38**, 4522 (2013).
- ⁴⁸ J. Kasprzak, M. Richard, S. Kundermann, A. Baas, P. Jeambrun, J.M.J. Keeling, F.M. Marchetti, M.H. Szymńska, R. André, J.L. Staehli, V. Savona, P.B. Littlewood, B. Deveaud, L.S. Dang, K.G. Lagoudakis, M. Wouters, M. Richard, A. Baas, I. Carusotto, R. André, L.S. Dang, B. Deveaud-Plédran, T. Ostatnický, A. V. Kavokin, Y.G. Rubo, R. André, B. Deveaud-Plédran, K.S. Daskalakis, S.A. Maier, R. Murray, and S. Kéna-Cohen, *Nature* **13**, 409 (2008).
- ⁴⁹ M.O. Scully and M.S. Zubairy, *Quantum Optics* (Cambridge University Press, 1997).
- ⁵⁰ H. Deng, G.S. Solomon, R. Hey, K.H. Ploog, and Y. Yamamoto, *Phys. Rev. Lett.* **99**, 1 (2007).
- ⁵¹ M. Born and E. Wolf, *Principles of Optics: Electromagnetic Theory of Propagation, Interference and Diffraction of Light* (Cambridge University Press, 2006).
- ⁵² T. Aichele, G. Reinaudi, and O. Benson, *Phys. Rev. B - Condens. Matter Mater. Phys.* **70**, 1 (2004).
- ⁵³ A. Ulhaq, S. Weiler, S.M. Ulrich, R. Roßbach, M. Jetter, and P. Michler, *Nat. Photonics* **6**, 238 (2012).
- ⁵⁴ J.S. Cohen and D. Lenstra, *IEEE J. Quantum Electron.* **25**, 1143 (1989).
- ⁵⁵ D. Lenstra, B.H. Verbeek, and A.J. den Boef, *IEEE J. Quantum Electron.* **21**, 674 (1985).
- ⁵⁶ K.G. Lagoudakis, M. Wouters, M. Richard, A. Baas, I. Carusotto, R. André, L.S. Dang, and B. Deveaud-Plédran, *Nat. Phys.* **4**, 706 (2008).